双层花状光学涡旋晶格产生及特性研究

韩冰，樊海豪，凡梦然，景晓楠，温冰艳，李新忠*

河南科技大学物理工程学院，河南 洛阳 471023

摘要　利用束腰半径不同的奇模和偶模因斯高斯光束同轴叠加，产生了一种双层花状光学涡旋晶格，通过实验与数值模拟对所提出的双层花状光学涡旋晶格进行分析研究。结果表明：由束腰半径不同的奇模和偶模因斯高斯光束叠加而成的光学涡旋晶格中的涡旋呈单层或双层分布，且不同层涡旋点的拓扑荷值大小相等，符号相反；当奇偶模因斯高斯光束之间的束腰半径差距逐渐减小，涡旋分布由双层变为单层；此外，可以通过改变奇偶模因斯高斯光束之间的相位差，实现涡旋符号的调控。该研究结果极大地丰富了光学涡旋晶格的空间模式分布，在微粒操纵领域有着潜在应用。

关键词　物理光学；因斯高斯光束；光学涡旋晶格；微粒操纵

1 引　　言

由于携带了轨道角动量这一自由度[1]，近年来，涡旋光束成为了空间结构光场领域的研究热点，广泛应用于微粒操纵[2-5]、量子信息编码[6-7]、光学成像[8-10]、光学测量[11-14]、光通信[15-18]等领域。而光学涡旋晶格由于包含多个光学涡旋，具有更大的灵活性和潜在的应用前景，也得到了广泛研究[19-23]。

作为空间近轴波动方程在椭圆坐标系下的准确正交解，Ince-Gaussian（IG）光束包含奇模和偶模，横向强度分布丰富[24]，叠加产生的光学涡旋晶格具有额外的丰富结构。文献[25]利用道威棱镜构成的 Mach-Zehnder 干涉仪将相同的 IG 模式叠加，产生了一种矩形光学涡旋晶格。文献[26]利用一种新型宽口径激光二极管抽运薄片固态激光器，产生了径向和矩形的光学涡旋晶格。文献[27]使用大孔径离轴泵浦 Yb∶CALGO 激光器，在横向锁模状态下产生结构可变的光学涡旋晶格。然而，上述产生方法较为复杂，且产生的光学涡旋晶格难以自由调制。文献[28]基于计算全息法，利用特定参数的奇偶模 IG 光束叠加产生了一种涡旋数量和结构可

控的光学涡旋晶格，但没有进一步研究束腰半径对 IG 光束叠加产生的光学涡旋晶格的影响。

针对以上问题，本文利用束腰半径不同的奇偶模 IG 光束叠加，实验产生了一种双层花状光学涡旋晶格（DFOVL），分析了束腰半径对该双层光学涡旋晶格模式分布的影响，并且通过在奇偶模 IG 光束之间添加相位差，可以调控涡旋点的符号，实现涡旋点的产生与消失。

2 理论基础

IG 光束是空间近轴波动方程在椭圆坐标系下的正交解，沿光轴传输距离为 z 的截面上，定义椭圆坐标系为 $x=f(z)\cosh\xi\cos\eta$，$y=f(z)\sinh\xi\sin\eta$，其中 $\xi\in(0,\infty)$ 为径向椭圆变量，$\eta\in(0,2\pi)$ 为角向椭圆变量，$f(z)=f_0\omega(z)/\omega$ 为椭圆半焦距（f_0 和 ω 分别为 $z=0$ 截面处的半焦距和高斯光束的束腰半径），波长为 λ 的高斯光束的截面宽度在 z 轴上服从 $\omega(z)=\omega(1+z^2/z_R^2)^{1/2}$ 分布，$z_R=k\omega^2/2$ 是瑞利长度，k 为波数。在此椭圆坐标系下求解得到的奇模和偶模 IG 光束复振幅表达式如下所示[29]：

$$\mathrm{IG}_{p,m}^{\mathrm{o}}(r,\varepsilon)=\frac{S\omega}{\omega_{\mathrm{o}}(z)}S_p^m(\mathrm{i}\xi,\varepsilon)S_p^m(\eta,\varepsilon)\exp\left[\frac{-r^2}{w_{\mathrm{o}}^2(z)}\right]\exp\left\{\mathrm{i}\left[kz+\frac{kr^2}{2R(z)}-(p+1)\right]\Psi_{\mathrm{GS}}(z)\right\}, \tag{1}$$

$$\mathrm{IG}_{p,m}^{\mathrm{e}}(r,\varepsilon)=\frac{C\omega}{\omega_{\mathrm{e}}(z)}C_p^m(\mathrm{i}\xi,\varepsilon)C_p^m(\eta,\varepsilon)\exp\left[\frac{-r^2}{w_{\mathrm{e}}^2(z)}\right]\exp\left\{\mathrm{i}\left[kz+\frac{kr^2}{2R(z)}-(p+1)\right]\Psi_{\mathrm{GS}}(z)\right\}, \tag{2}$$

式中：上标 o 和 e 分别表示奇模和偶模 IG 光束；r 为径向位置矢量大小；$\varepsilon=2f_0^2/\omega^2$ 为椭圆参数；p 和 m 分别为奇偶模 IG 光束的阶数和级数，满足 $1\leqslant m\leqslant p$ 和 $(-1)^{p-m}=1$；C 和 S 为归一化参数；$S_p^m(\eta,\varepsilon)$ 和 $C_p^m(\eta,\varepsilon)$ 分别表示奇模和偶模的因斯多项式；$R(z)$ 为高斯光束波前曲率半径，$R(z)=z[1+(z_R/z)^2]$；$\Psi_{GS}(z)$ 为 Gouy 相移，$\Psi_{GS}(z)=\arctan(z/z_R)$；$w_o(z)$ 为奇模 IG 光束的束腰半径；$w_e(z)$ 为偶模 IG 光束的束腰半径。

在本文中，利用阶数和级数分别相同、束腰半径不同的奇模和偶模 IG 光束同轴干涉叠加，产生了一种含有双层暗核的光学涡旋晶格（DFOVL），其复振幅的表达式为

$$A_{DFOVL}=IG^e_{m+2,m,w_e}(\xi,\eta,\varepsilon)\exp(i\varphi)+$$
$$IG^o_{m+2,m,w_o}(\xi,\eta,\varepsilon), \quad (3)$$
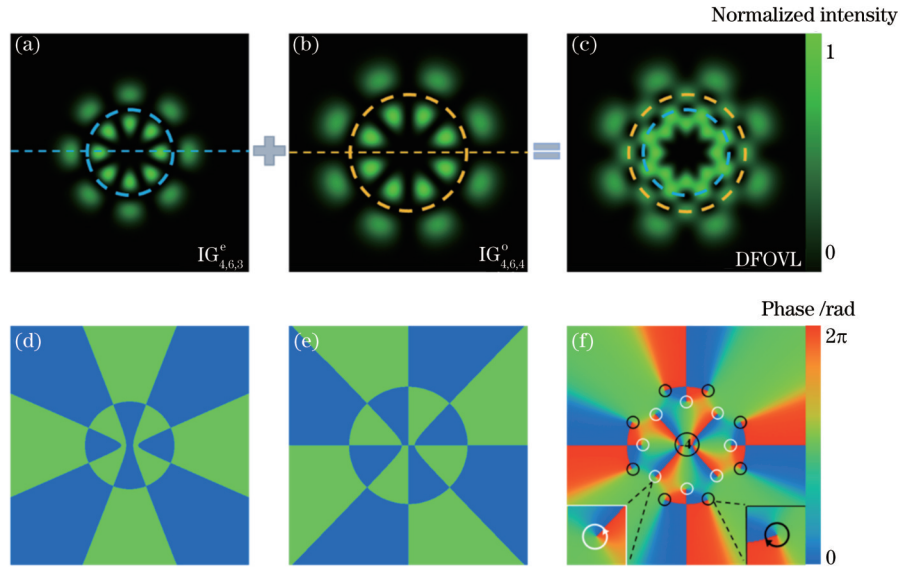
式中：φ 是奇偶模 IG 光束之间的初始相位差。模拟分析要求阶数 p 和级数 m 之间满足 $p=m+2$。

图 1　DFOVL 的产生过程。(a)(d) $IG^e_{4,6,3}$ 的模拟光强图和相位图；(b)(e) $IG^o_{4,6,4}$ 的模拟光强图和相位图；(c)(f) DFOVL 的模拟光强图和相位图

Fig. 1　Generation process of DFOVL. (a)(d) Simulated intensity pattern and phase pattern of $IG^e_{4,6,3}$, respectively; (b)(e) simulated intensity pattern and phase pattern of $IG^o_{4,6,4}$, respectively; (c)(f) simulated intensity pattern and phase pattern of DFOVL, respectively

图 1 是以 $\varepsilon=1/8$、$m=4$、$\varphi=0$ 为例的 DFOVL 产生过程，其中奇模 IG 光束的束腰半径 $w_o=4$ mm，偶模 IG 光束的束腰半径 $w_e=3$ mm。图 1(a)、(b) 分别是偶模 IG 光束和奇模 IG 光束的模拟光强图，图 1(c) 是由不同束腰半径的奇偶模 IG 光束叠加产生的光学涡旋晶格的模拟光强图，图中两个虚线圈为内外两层暗核所在位置。由图 1(c) 可以看出，该光学涡旋晶格中内外两层暗核均呈现圆形分布，内外层暗核数量相等，均为 8 个，暗核总数满足 $N=4m$ 的关系，图 1(f) 为其对应的相位图[插图分别是正涡旋和负涡旋的 3 倍放大图，圆形箭头表示相位增加的方向]。图 1(f) 中黑色圆环和白色圆环标记处是暗核所在位置，定义：白色圆环为正涡旋，即相位从 0 逆时针增至 2π；黑色圆环表示负涡旋，即相位从 0 顺时针增加至 2π[30]。由图 1(f) 可以看出，该光学涡旋晶格上的内外两层暗核处存在涡旋点，内外两层涡旋点拓扑荷符号相反，大小相等，且光学涡旋晶格中心的大暗核处同样存在拓扑荷值为 -4 的涡旋点。为便于研究，本文重点关注该光学涡旋晶格中四周的子涡旋点。

3　实验

产生该 DFOVL 的实验装置图如图 2 所示，由 Nd:YAG 激光器经倍频生成的 532 nm 的光束经过针孔滤波器（PF）和凸透镜 L1（焦距 $f_1=100$ mm）后得到平行光，平行光经过起偏器 P 起偏后通过分束立方体 BS1，一束光照射在用于加载相位掩模版的空间光调制器（SLM，HOLOEYE，PLUTO-VIS-016，像素大小为 8 μm×8 μm）上，相位掩模版记录了 DFOVL 的相位和振幅信息，经空间光调制器调制后的光束经配合光阑 A2 的 4f（焦距 $f_2=200$ mm，$f_3=200$ mm）系统后，筛选出所需的 +1 级衍射光束，最后由放置在透镜 L3 的后焦平面上的 CCD 照相机（Basler acA1600-60gc，像素大小为 4.5 μm×4.5 μm）记录其强度分布。另一束光通过透镜 L4（焦距 $f_4=75$ mm）转换成球面波，与产生的 DFOVL 同轴干涉。

4　实验结果与讨论

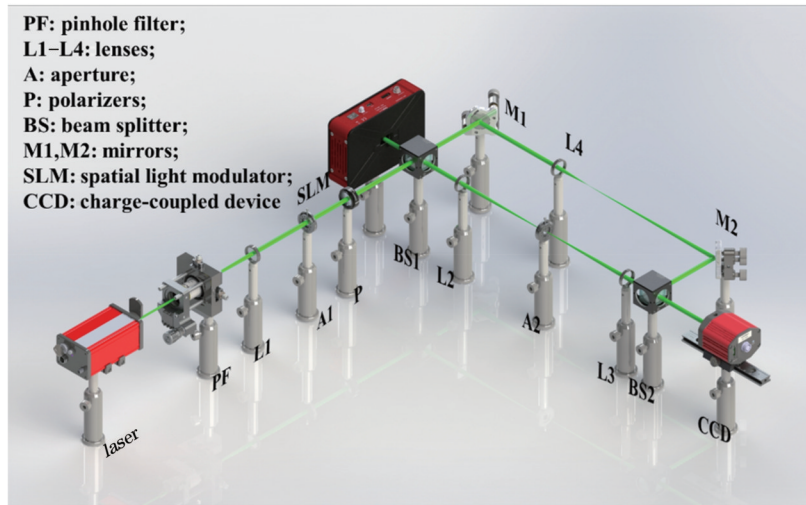基于上述实验装置，令初始相位差 $\varphi=0$，椭圆参数均为 $\varepsilon=1/8$、$w_e=3$ mm、$w_o=4$ mm，实验生成了该

图 2 实验装置原理图

Fig. 2 Schematic of experimental setup

光学涡旋晶格，如图 3 所示。图 3(a1)~(d1)和图 3 (a2)~(d2)分别是当 $m=1,2,3,4$ 生成的 DFOVL 的实验光强图和模拟光强图，图 3(a2)~(d2)中的插图是实验所用的相位掩模版。通过计算实验光强图与模拟光强图之间的相关系数，即模式纯度 R[31]，验证实验图的质量，模式纯度的值如图 3(a1)~(d1)所示。由于中心区域亮度较大，光学涡旋晶格中外围的光瓣弱到无法被观测到，然而，模式纯度仍然大于 0.8，说明实验

生成了质量较好的 DFOVL。实际上，相位掩模版的设计参数会影响输出光束的模式纯度[32]，如果研究人员需要更高质量的光束来观察更多的细节，则需要对相位掩模版进行进一步优化。

由图 3(a1)~(d1)可以看出，随着级数 m 的增大，暗核数量逐渐增多，其暗核数量分别为 4、8、12 和 16，暗核的数量 N 满足 $N=4m$。图 3(a2)~(d2)中虚线为暗核所在位置。当 $m=1$ 时，暗核呈椭圆形单层
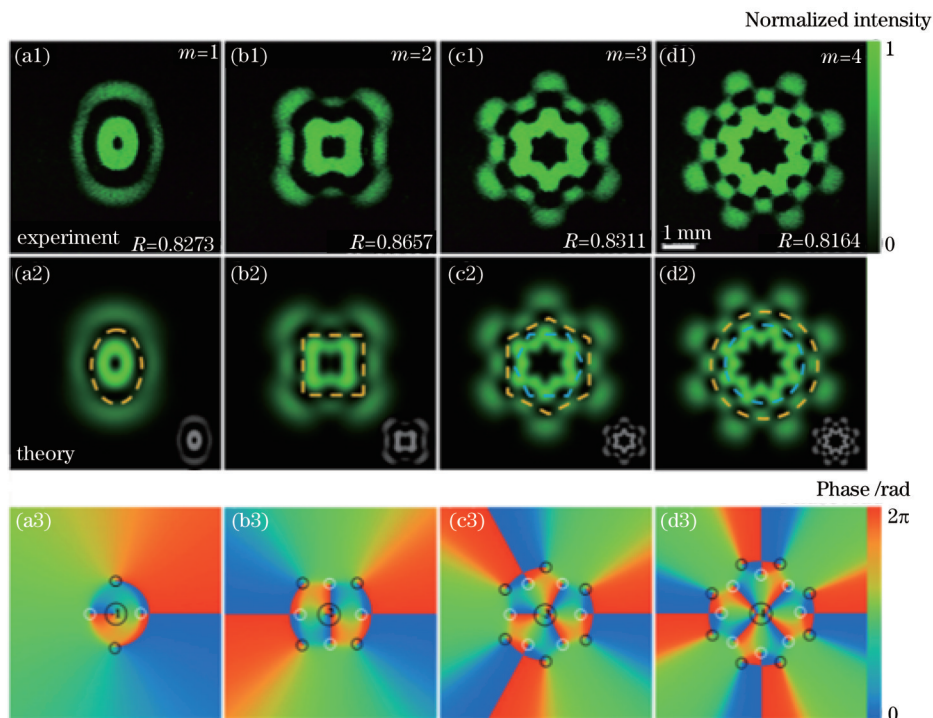

图 3 不同级数 m 下 DFOVL 的光强图和相位图。(a1)~(d1) DFOVL 的实验光强图；(a2)~(d2) DFOVL 的模拟光强图(插图是实验所用的相位掩模版)；(a3)~(d3) DFOVL 的模拟相位图

Fig. 3 Intensity distributions and phase distributions of DFOVLs with different level m. (a1)-(d1) Experimental intensity patterns of DFOVLs; (a2)-(d2) simulated intensity patterns of DFOVLs [Insets are phase masks used in experiments]; (a3)-(d3) simulated phase patterns of DFOVLs

分布;当 $m=2$ 时,暗核沿矩形单层分布;当 $m=3$ 时,暗核呈双层分布,内层与外层暗核沿正六边形分布;当 $m=4$ 时,暗核同样呈双层分布,且内层与外层暗核均沿圆形分布。图 3(a3)~(d3)分别是 $m=1,2,3,4$ 时光学涡旋晶格的模拟相位图,由图可以看出,该光学涡旋晶格中同时存在正涡旋和负涡旋,中心大暗核拓扑荷值 $T_c=-m$。而对于四周的涡旋点,正涡旋数量和负涡旋数量相等,每个涡旋点拓扑荷值大小为 1。

当 $m=1,2$,正负涡旋存在于同一层;当 $m=3,4$ 且暗核呈双层分布时,内外层涡旋点数量相等,拓扑荷值符号相反。此外,该花状光学涡旋晶格的很多性质都保留着 IG 光束的性质,例如:奇偶模式空间不重合位

置的光强分布以及光束的传输特性[25]等。

为验证生成的光学涡旋晶格存在涡旋相位,本文利用图 3(a1)~(d1)产生的光学涡旋晶格与球面波进行干涉。如图 4 所示,第一行为实验干涉图,第二行为模拟干涉图。根据光学涡旋的性质,其与球面波发生干涉时将会在暗核处出现叉丝,叉丝按照顺时针方向增加为正涡旋,逆时针方向增加为负涡旋,叉丝变化的数量表示拓扑荷值大小。由图 4(a1)~(d1)可知,每个暗核处都存在分叉,分叉区域数量满足 $N=4m$ 的关系,且中心区域的螺旋条纹数量分别为 1、2、3、4,周围暗核处叉丝变化数量都为 1,证明每个暗核处都存在涡旋点,且中心暗核拓扑荷值大小等于 m,四周暗核拓扑荷值大小等于 1。
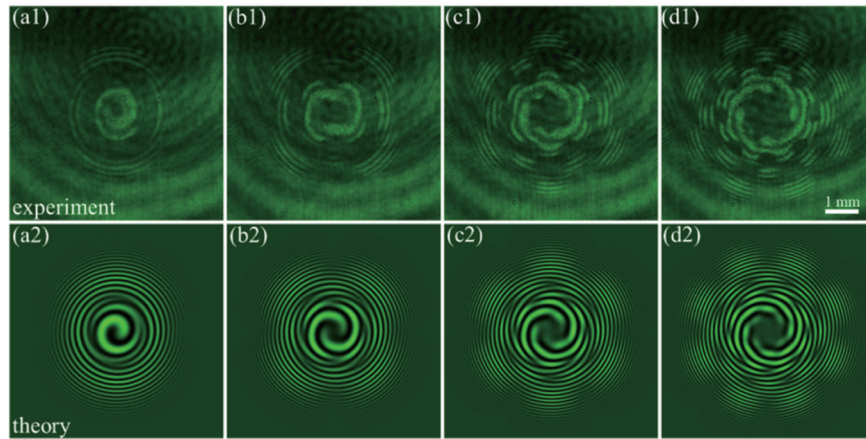

图 4 DFOVL 与球面波的干涉图。(a1)~(d1)实验生成的 DFOVL 与球面波干涉图;(a2)~(d2)模拟生成的 DFOVL 与球面波干涉图

Fig. 4 Interference patterns between DFOVLs and spherical wave. (a1)-(d1) Experimental interference patterns between spherical wave and DFOVLs; (a2)-(d2) simulated interference patterns between spherical wave and DFOVLs

为了研究束腰半径对该光学涡旋晶格的光强分布影响,本文以 $m=4$、$\varphi=0$、$\varepsilon=1/8$ 的 DFOVL 为例,将束腰半径不同的奇模和偶模 IG 光束同轴叠加,如图 5 所示。其中,图 5(a1)~(a6)和图 5(b1)~(b6)分别是当奇模束腰半径 $w_o=4$ mm 时,偶模束腰半径 w_e 从 3 mm 每隔 0.2 mm 增大到 4 mm 时叠加产生的 DFOVL 的实验光强图和对应的球面波干涉。图 5(a7)~(a12)和图 5(b7)~(b12)分别是当偶模束腰半径 $w_e=4$ mm 时,奇模束腰半径 w_o 从 3 mm 每隔 0.2 mm 增大到 4 mm 时叠加产生的 DFOVL 的实验光强图和对应的球面波干涉图。图 5(a1)~(a12)中的插图是实验所用的相位掩模版。

由图 5(a1)~(a6)可知:当奇模束腰半径 w_o 保持不变,随着偶模 IG 光束的束腰半径 w_e 逐渐增大,内外层边缘凸起逐渐平缓,光强分布趋于圆环状,奇模和偶模 IG 光束之间的束腰半径差距越小,变化趋势越明显;当奇模和偶模 IG 光束的束腰半径相等时,光强分布呈现光滑的同心圆环。由图 5(b1)~(b6)所示的球面波干涉图可以看出:当 $w_e \neq w_o$ 时,虽然光强分布不

同,但涡旋数量始终满足 $N=4m$,且随着奇模和偶模 IG 光束之间的束腰半径差距变小,涡旋逐渐由双层分布变为单层分布,涡旋拓扑荷值大小和符号保持不变;当 $w_e=w_o$ 时,该光学涡旋晶格中周围暗核消失,仅存在中心大暗核。图 5(a7)~(a12)所示的双层花状光学涡旋晶格的实验光强分布与图 5(a1)~(a6)相比旋转了 $\pi/4$,光强和涡旋点分布变化趋势与上述类似,这里不再赘述。

为了研究初始相位差对 DFOVL 的调控特性,本文以 $m=4$、$w_e=3$ mm、$w_o=4$ mm、$\varepsilon=1/8$ 的 DFOVL 为例,给偶模 IG 光束添加相位差 φ,得到了当 φ 从 0 增加到 2π 时 DFOVL 的实验光强图和对应的球面波干涉图,如图 6 所示。由图 6(a1)~(a4)可以看出:当 φ 从 0 增大到 $\pi/2$,光学涡旋晶格光强模式逐渐沿顺时针方向转变为 8 个光瓣,并且如图 6(a4)、(b4)所示,当初始相位差等于 $\pi/2$ 时形成了完全孤立的光瓣,此时暗核完全消失,相位奇点也相应消失。其次,随着初始相位差从 $\pi/2$ 增加到 π:由图 6(a4)~(a7)可以看出光学涡旋晶格光强模式逐渐沿逆时针方向恢复;由图 6(b4)~(b7)可
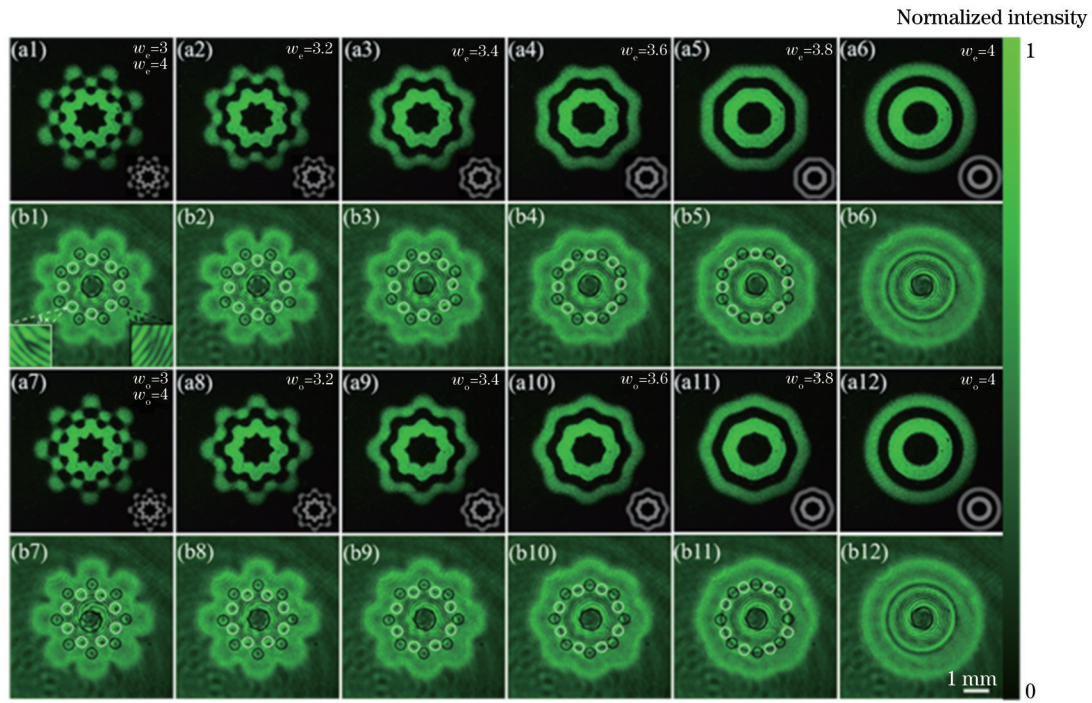
图 5　不同束腰半径下 DFOVL 的实验光强图和球面波干涉图[图 5(b1)中插图分别是正涡旋和负涡旋与球面波干涉的 3 倍放大图，图 5(a1)～(a12)中的插图是实验所用的相位掩模版]。(a1)～(a12) 实验光强图；(b1)～(b12)球面波干涉图

Fig. 5　Experimental intensity patterns and spherical wave interference patterns of DFOVLs at different waist radius [Insets in Fig. 5 (b1) are $3\times$ magnification of interference patterns between positive and negative optical vortex beams and spherical wave, respectively; insets in Figs. 5(a1)‒(a12) are phase masks used in experiments]. (a1)‒(a12) Experimental intensity patterns; (b1)‒(b12) spherical wave interference patterns

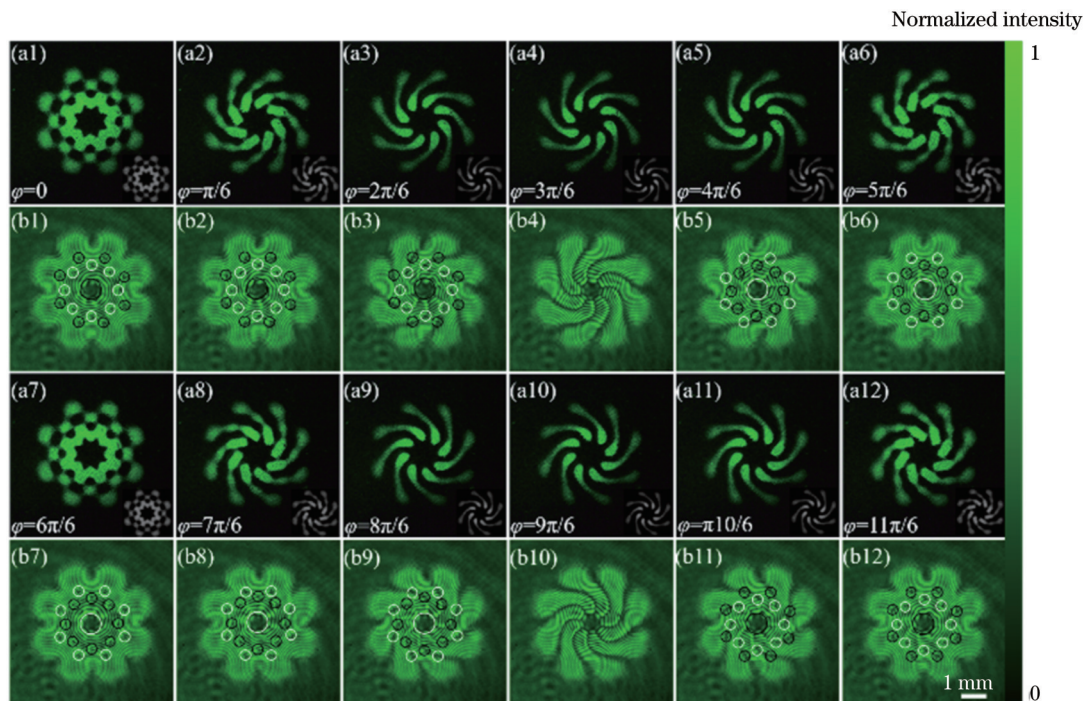图 6　不同相位差 φ 下 DFOVL 的光强和球面波干涉图。(a1)～(a12) DFOVL 的实验光强图(插图是实验所用的相位掩模版)；(b1)～(b12) DFOVL 与球面波干涉实验图

Fig. 6　Intensity distributions and spherical wave interference patterns of DFOVLs for different phase difference φ. (a1)‒(a12) Experimental intensity patterns of DFOVLs (insets are phase masks used in experiments); (b1)‒(b12) experimental interference patterns between spherical wave and DFOVLs

知,此时光学涡旋晶格中涡旋点由正涡旋变为负涡旋,或者由负涡旋变为了正涡旋。因此,通过调控奇偶模 IG 光束的初始相位差可以调控涡旋点的符号。当初始相位差等于 $3\pi/2$ 时,由图 6(a10)和(b10)可以看出相位奇异点再次消失,光强模式变为完全孤立的光瓣,并呈逆时针旋转。最后,当初始相位差从 $3\pi/2$ 增加到 2π 时,由图 6(a10)~(a12)可以看出光学涡旋晶格光强模式沿顺时针方向恢复,并且涡旋符号再次改变。此外,当在奇模 IG 光束中引入初始相位差,该变化过程与上述过程相反。因此,通过调控奇偶模 IG 光束之间的相位差可以改变 DFOVL 的涡旋符号,这在量子信息编码和多微粒操纵等领域具有重要意义。

5 结 论

实验产生了一种由束腰半径不同的奇偶模 IG 光束叠加而成的双层花状光学涡旋晶格,该光学涡旋晶格中涡旋呈双层分布,涡旋数量 N 满足 $N=4m$,并且内外层涡旋拓扑荷值大小相等,符号相反。研究了束腰半径和相位差对其光强及相位分布的影响。结果表明:当奇偶模 IG 光束之间的相位差 φ 为 π 的整数倍时,涡旋符号发生改变;当 φ 为 $\pi/2$ 的奇数倍时,涡旋点消失。因此可以通过改变相位差调控涡旋点符号以及实现涡旋点的产生与消失。当奇偶模因斯高斯光束之间的束腰半径差距逐渐减小,叠加产生的双层光学涡旋晶格光强分布逐渐趋于同心圆环,且涡旋暗核分布由双层变为单层。该研究结果丰富了光学涡旋晶格的空间模式,在微粒操控领域具有潜在的应用价值。

参 考 文 献

[1] Allen L, Beijersbergen M W, Spreeuw R J, et al. Orbital angular momentum of light and the transformation of Laguerre-Gaussian laser modes[J]. Physical Review A, 1992, 45(11): 8185-8189.

[2] Zhu L H, Tang M M, Li H H, et al. Optical vortex lattice: an exploitation of orbital angular momentum[J]. Nanophotonics, 2021, 10(9): 2487-2496.

[3] Long Z X, Zhang H, Tai Y P, et al. Optical vortex array with deformable hybrid Ferris structures[J]. Optics & Laser Technology, 2022, 145: 107524.

[4] Li X Z, Ma H X, Zhang H, et al. Is it possible to enlarge the trapping range of optical tweezers via a single beam?[J]. Applied Physics Letters, 2019, 114(8): 081903.

[5] 朱刘昊, 秦雪云, 台玉萍, 等. 摆线光束的微粒等间距操控(特邀)[J]. 红外与激光工程, 2021, 50(9): 20210380.
Zhu L H, Qin X Y, Tai Y P, et al. Equal spacing control of particle via cycloidal beam (Invited)[J]. Infrared and Laser Engineering, 2021, 50(9): 20210380.

[6] Wang J, Yang J Y, Fazal I M, et al. Terabit free-space data transmission employing orbital angular momentum multiplexing[J]. Nature Photonics, 2012, 6(7): 488-496.

[7] 阎思瑾, 张冬凯, 陈理想. 光子径向模式:光场调控及量子信息应用进展[J]. 光学学报, 2022, 42(3): 0327002.
Yan S J, Zhang D K, Chen L X. Photonic radial modes: progress in light field manipulation and quantum information applications[J]. Acta Optica Sinica, 2022, 42(3): 0327002.

[8] Lavery M P J, Speirits F C, Barnett S M, et al. Detection of a

[9] spinning object using light's orbital angular momentum[J]. Science, 2013, 341(6145): 537-540.

[9] Qiu X D, Li F S, Zhang W H, et al. Spiral phase contrast imaging in nonlinear optics: seeing phase objects using invisible illumination[J]. Optica, 2018, 5(2): 208-212.

[10] 杨伟东, 邱晓东, 陈理想. 光轨道角动量分离、成像、传感及微操控应用研究进展[J]. 中国激光, 2020, 47(5): 0500013.
Yang W D, Qiu X D, Chen L X. Research progress in detection, imaging, sensing, and micromanipulation application of orbital angular momentum of beams[J]. Chinese Journal of Lasers, 2020, 47(5): 0500013.

[11] Li X Z, Tai Y P, Zhang L P, et al. Characterization of dynamic random process using optical vortex metrology[J]. Applied Physics B, 2014, 116(4): 901-909.

[12] Yu W T, Ji Z H, Dong D S, et al. Super-resolution deep imaging with hollow Bessel beam STED microscopy[J]. Laser & Photonics Reviews, 2016, 10(1): 147-152.

[13] Fu S Y, Wang T L, Zhang Z Y, et al. Non-diffractive Bessel-Gauss beams for the detection of rotating object free of obstructions[J]. Optics Express, 2017, 25(17): 20098-20108.

[14] Zhai Y W, Fu S Y, Yin C, et al. Detection of angular acceleration based on optical rotational Doppler effect[J]. Optics Express, 2019, 27(11): 15518-15527.

[15] Fu S Y, Zhai Y W, Zhou H, et al. Demonstration of free-space one-to-many multicasting link from orbital angular momentum encoding[J]. Optics Letters, 2019, 44(19): 4753-4756.

[16] 郭忠义, 龚超凡, 刘洪郡, 等. OAM 光通信技术研究进展[J]. 光电工程, 2020, 47(3): 90-123.
Guo Z Y, Gong C F, Liu H J, et al. Research advances of orbital angular momentum based optical communication technology[J]. Opto-Electronic Engineering, 2020, 47(3): 90-123.

[17] 南久航, 韩一平. 双路多进制涡旋光通信[J]. 光学学报, 2021, 41(12): 1206001.
Nan J H, Han Y P. Dual-channel multiband vortex optical communication[J]. Acta Optica Sinica, 2021, 41(12): 1206001.

[18] Fu S Y, Zhai Y W, Zhou H, et al. Experimental demonstration of free-space multi-state orbital angular momentum shift keying[J]. Optics Express, 2019, 27(23): 33111-33119.

[19] Li X Z, Zhang H. Anomalous ring-connected optical vortex array[J]. Optics Express, 2020, 28(9): 13775-13785.

[20] 李伟, 俞嘉文, 闫爱民. 涡旋激光阵列产生技术研究进展[J]. 激光与光电子学进展, 2020, 57(9): 090002.
Li W, Yu J W, Yan A M. Research progress of vortex beam array generation technology[J]. Laser & Optoelectronics Progress, 2020, 57(9): 090002.

[21] Franke-Arnold S, Leach J, Padgett M J, et al. Optical Ferris wheel for ultracold atoms[J]. Optics Express, 2007, 15(14): 8619-8625.

[22] Vasilyeu R, Dudley A, Khilo N, et al. Generating superpositions of higher-order Bessel beams[J]. Optics Express, 2009, 17(26): 23389-23395.

[23] 秦雪云, 朱刘昊, 台玉萍, 等. 多平面波干涉的光学涡旋晶格特性研究[J]. 光学学报, 2021, 41(21): 2126001.
Qin X Y, Zhu L H, Tai Y P, et al. Properties of optical vortex lattice generated via multiple plane wave interference[J]. Acta Optica Sinica, 2021, 41(21): 2126001.

[24] 张明明, 白胜闯, 董俊. Ince-Gaussian 模式激光的研究进展[J]. 激光与光电子学进展, 2016, 53(2): 020002.
Zhang M M, Bai S C, Dong J. Advances in Ince-Gaussian modes laser[J]. Laser & Optoelectronics Progress, 2016, 53(2): 020002.

[25] Chu S C, Yang C S, Otsuka K. Vortex array laser beam generation from a Dove prism-embedded unbalanced Mach-Zehnder interferometer[J]. Optics Express, 2008, 16(24): 19934-19949.

[26] Otsuka K, Chu S C. Generation of vortex array beams from a

thin-slice solid-state laser with shaped wide-aperture laser-diode pumping[J]. Optics Letters, 2009, 34(1): 10-12.

[27] Shen Y J, Wan Z S, Fu X, et al. Vortex lattices with transverse-mode-locking states switching in a large-aperture off-axis-pumped solid-state laser[J]. Journal of the Optical Society of America B, 2018, 35(12): 2940-2944.

[28] Fan H H, Zhang H, Cai C Y, et al. Flower-shaped optical vortex array[J]. Annalen Der Physik, 2021, 533(4): 2000575.

[29] Bandres M A, Gutiérrez-Vega J C. Ince-Gaussian beams[J]. Optics Letters, 2004, 29(2): 144-146.

[30] Li L, Chang C L, Yuan X Z, et al. Generation of optical vortex array along arbitrary curvilinear arrangement[J]. Optics Express, 2018, 26(8): 9798-9812.

[31] Ohtake Y, Ando T, Fukuchi N, et al. Universal generation of higher-order multiringed Laguerre-Gaussian beams by using a spatial light modulator[J]. Optics Letters, 2007, 32(11): 1411-1413.

[32] Ando T, Ohtake Y, Matsumoto N, et al. Mode purities of Laguerre-Gaussian beams generated via complex-amplitude modulation using phase-only spatial light modulators[J]. Optics Letters, 2009, 34(1): 34-36.

Generation and Characteristics of Double-Layer Flower-Shaped Optical Vortex Lattice

Han Bing, Fan Haihao, Fan Mengran, Jing Xiaonan, Wen Bingyan, Li Xinzhong[*]

School of Physics and Engineering, Henan University of Science and Technology, Luoyang 471023, Henan, China

Abstract

Objective Due to the degree of freedom of orbital angular momentum, vortex beams have become a research hotspot in the field of spatially structured light fields in recent years, which are widely used in micro-particle manipulation, optical imaging, optical measurement, and optical communication. The wide application of this novel beam has also greatly stimulated researchers to explore and understand the structure of light fields. With the in-depth study of the new vortex field, researchers are no longer limited to the study of a single optical vortex, but focus on multiple optical vortices arranged according to a certain rule, namely the optical vortex lattice. In recent years, optical vortex lattices have been applied to optical measurements and show the promise of ultra-cold atoms trapping. Therefore, the generation and regulation of optical vortex lattice are of great scientific significance in related optical fields. So far, optical vortex lattices are usually generated by the superposition of two or more specific optical beams. Researchers have produced several optical vortex lattices via the superposition of Gaussian beams, Ince-Gaussian (IG) beams, Hermite-Gaussian beams, and Laguerre-Gaussian beams. Among these approaches, optical vortex arrays generated by the superposition of IG beams have additional abundant structures owing to the rich transverse intensity distribution of the IG beams. However, the influence of beam waist on the optical vortex lattice generated by IG beam superposition is not further studied. Therefore, it is necessary to study the characteristics of optical vortex lattice generated by IG superposition with different beam waist radii, so as to enrich the spatial pattern distribution of optical vortex lattice.

Methods In this paper, a double-layer flower-shaped optical vortex lattice is proposed by superimposing odd and even mode IG beams with different waist radii based on computational holography. The optical vortex lattice is successfully generated by single optical path interference method, and the existence of vortex phase in the generated optical vortex lattice is verified by spherical wave interference. The experimental setup is shown in Fig. 2. The 532 nm beam generated by Nd：YAG laser after frequency doubling passes through the pinhole filter and convex lens L1 (f_1＝100 mm) to obtain an expanded beam. The expanded beam is split into two beams after it passes through the beam splitter. One beam is illuminated on the spatial light modulator (SLM) used to load the phase mask (HOLOEYE, PLUTO-VIS-016, pixel size is 8 μm×8 μm). The phase mask records the phase and amplitude information of the double-layer flower-shaped optical vortex lattice. The beam modulated by the SLM is screened out by the $4f$ (f_2＝200 mm, f_3＝200 mm) system of aperture A2, and the required ＋1 order diffraction beam is finally recorded by CCD camera (Basler acA1600-60gc, pixel size is 4.5 μm×4.5 μm) placed in the back focal plane of lens L3. Another beam is converted into a spherical wave through the lens L4 (f_4＝75 mm).

Results and Discussions The optical vortex lattices are double-layer distribution, and the number of vortices N meets the relationship of $N＝4m$. And the topological charge values of the inner and outer vortices equal, but the signs are opposite (Fig. 3). The spherical wave interferes with the optical vortex lattice. According to the properties of the optical vortex, when it interferes with the spherical wave, a fork filament appears at the dark core, therefore verifying the vortex phase of the producing optical vortex lattice (Fig. 4). In order to research the effect of waist radius on the light intensity distribution

of the optical vortex lattice, the odd mode waist radius $w_o=4$ mm is controlled. When the even mode IG beam waist radius increases from 3 mm to 4 mm with a step of 0.2 mm, the inner and outer edge bulges gradually flatten and the intensity distribution intends to be circular. As the waist radius gap between the odd and even mode IG beams decreases, the vortex distribution gradually changes from double layer to single layer, and the topological charge values and signs remain unchanged. When the waist radii equal, the surrounding dark cores in optical vortex lattice disappear, and only the central large dark core exists (Fig. 5). To investigate the properties of initial phase difference of DFOVL, the phase difference φ is added to the even mode IG beams, forming a completely isolated light flap when the initial phase difference is equal to $\pi/2$, which the dark cores and phase singular dots completely disappear. When the initial phase difference increases to π, the intensity mode of optical vortex lattice restores, but the signs of the inner and outer vortexes in the optical vortex lattice change (Fig. 6).

Conclusions We have experimentally produced a double-layer flower-shaped optical vortex lattice, which is generated by coaxial superposition of odd-mode and even-mode Ince-Gaussian beams with different waist radius. The distributions of vortices in optical vortex lattice are double-layer, the number of vortices N meets the relationship of $N=4m$, and the topological charge values of the inner and outer vortices equal, but the signs are opposite. The effects of waist radius and phase difference on the distribution characteristics of light intensity and phase are analyzed. The results show that: when the phase difference φ between the odd and even mode IG beams is an integer multiple of π, the vortex sign changes; when φ is an odd multiple of $\pi/2$, the vortex disappears. Therefore, the generation and disappearance of vortex or the modulation of the vortex sign can be realized by changing the phase difference. When the waist radius gap between the odd mode and even mode IG beams gradually decreases, the light intensity distribution of the double-layer optical vortex lattice generated by superposition gradually intends to a concentric annulus, and the distribution of the vortex dark core changes from double-layer to single-layer. The research results greatly enrich the spatial mode distributions of optical vortex lattice and have potential applications in micro-particle manipulation.

Key words physical optics; Ince-Gaussian beams; optical vortex lattice; micro-particle manipulation